

Hemodynamic Characterization of Peripheral Arterio-venous Malformations

SABRINA FREY ¹, A. HAINE,² R. KAMMER,² H. VON TENG-G-KOBLIGK,³ D. OBRIST,¹ and I. BAUMGARTNER²

¹ARTORG Center for Biomedical Engineering Research, University of Bern, Murtenstrasse 50, 3008 Bern, Switzerland;

²Division of Angiology, Swiss Cardiovascular Center, University of Bern, Bern University Hospital, Bern, Switzerland; and

³Department of Diagnostic, Interventional and Pediatric Radiology, University of Bern, Bern University Hospital, Bern, Switzerland

(Received 23 December 2016; accepted 15 March 2017)

Associate Editor Kerry Hourigan oversaw the review of this article.

Abstract—Peripheral arterio-venous malformations (pAVMs) are congenital vascular anomalies that require treatment, due to their severe clinical consequences. The complexity of lesions often leads to misdiagnosis and ill-planned treatments. To improve disease management, we developed a computational model to quantify the hemodynamic effects of key angioarchitectural features of pAVMs. Hemodynamic results were used to predict the transport of contrast agent (CA), which allowed us to compare our findings to digital subtraction angiography (DSA) recordings of patients. The model is based on typical pAVM morphologies and a generic vessel network that represents realistic vascular feeding and draining components related to lesions. A lumped-parameter description of the vessel network was employed to compute blood pressure and flow rates. CA-transport was determined by coupling the model to a 1D advection–diffusion equation. Results show that the extent of hemodynamic effects of pAVMs, such as arterial steal and venous hypertension, strongly depends on the lesion type and its vascular architecture. Dimensions of shunting vessels strongly influence hemodynamic parameters. Our results underline the importance of the dynamics of CA-transport in diagnostic DSA images. In this context, we identified a set of temporal CA-transport parameters, which are indicative of the presence and specific morphology of pAVMs.

Keywords—Lumped parameter model, Blood flow modelling, Contrast agent transport, 1D advection–diffusion, Yakes AVM classification, Vascular malformations.

ABBREVIATIONS

AVM	Arterio-venous malformation
cAVM	Cerebral arterio-venous malformation
pAVM	Peripheral arterio-venous malformation
MR	Magnetic resonance
DSA	Digital subtraction angiography
CA	Contrast agent
LPM	Lumped parameter model
ATA	Anterior tibial artery
PTA	Posterior tibial artery
FbA	Fibular artery
MDA	Medial and dorsal arteries in the foot
DA	Digital arteries in the foot
DV	Digital veins in the foot
MDV	Medial and dorsal veins in the foot
PTV	Posterior tibial vein
ATV	Anterior tibial vein
FbV	Fibular vein
GSV	Great saphenous vein
SSV	Small saphenous vein
CO	Cardiac output

INTRODUCTION

Congenital vascular malformations are localized defects in embryonic vascular morphogenesis.⁴ Malformations can affect the arterial, venous and lymphatic system, or they can represent a combination of pathologies in between the systems. Arterio-venous malformations (AVMs) are high-flow malformations composed of an anomalous network of low-resistance blood vessels that connects the arterial and venous systems, bypassing the capillary bed.³⁰ AVMs are

Address correspondence to Sabrina Frey, ARTORG Center for Biomedical Engineering Research, University of Bern, Murtenstrasse 50, 3008 Bern, Switzerland. Electronic mail: sabrina.frey@artorg.unibe.ch

categorized as orphan's disease with a prevalence of about three per 10,000 individuals^{2,34} and are one of the most challenging vascular lesions to be diagnosed and treated, since the small number of affected patients leads to a lack of experience.³⁸ AVMs can occur in any part of the body, including the brain, lung,²⁸ muscle and bone.³⁷ Cerebral AVMs (cAVMs) are associated with epilepsy, neurological deficits, and most importantly, with a high risk of intracranial bleeding.¹⁹ Several studies used computational modelling to investigate hemodynamic processes^{16,20} and treatment effects²⁶ or to assess the risk of intracranial hemorrhage caused by cAVM rupture,^{14,19} all with a strong focus on angioarchitectures and treatment strategies inherent to cAVMs.

Peripheral AVMs (pAVMs) are located outside of the head, neck, and spine. pAVMs are rare but can be or become large and extremely complex.³⁷ They may require extensive treatment due to their potentially high impact on local tissue structures and the cardiovascular system.³⁶ To our knowledge, little theoretical research has been conducted to address the challenges faced by clinicians in characterizing and treating pAVMs.

Clinical effects are arterial steal and venous hypertension, both induced by a reduced flow resistance of pAVMs, which are competing for blood flow with the capillary bed. These effects lead to reduced perfusion within parallel capillary beds and impaired venous drainage from surrounding tissues, since capillary outflow veins encounter arterialized veins with abnormally elevated blood pressure. In severe cases, AVMs can lead to high-output cardiac failure³⁶ due to relevant arterio-venous shunting. Diagnosis is based on clinical findings, duplex ultrasound, non-invasive magnetic resonance (MR) imaging, and minimally-invasive intra-arterial digital subtraction angiography (DSA).²⁵ There is limited quantitative information on blood flow rates and pressure for individual pAVMs, although hemodynamic characteristics are important for prognosis.

The complexity of lesions often leads to ill-planned treatments and high complication rates, especially when performed by inexperienced physicians.³⁸ The Yakes classification system^{36,38} (Fig. 1) has been proposed to systematically determine appropriate pAVM management based on the lesion angioarchitecture. Although this classification is straightforward, it is a simplification of a complex hemodynamic pathology. As various types of AVMs go along with dedicated hemodynamic changes, a precise determination of these changes may ease classification and thereby treatment decisions if applicable on routine diagnostic tools.

We propose a computational model to identify and quantify hemodynamic effects of key angioarchitectural features of different pAVM types. Additionally, we aim at identifying diagnostic parameters indicative of the presence and type of pAVM. This set of diagnostic parameters shall be measurable with existing diagnostic modalities (e.g., MR, DSA) to establish a link between pAVM morphology, its hemodynamic consequences, and their manifestation in diagnostic images. Our model shall improve disease identification, classification, and therefore treatment selection and safety. It is a first step towards a clinical tool that may also support the education of medical practitioners and advance the prevailing experience-based diagnostic approach to a more deliberate, quantitative diagnostic procedure.

MATERIALS AND METHODS

The main elements of our model are depicted in Fig. 2 and introduced in the following sections. The computational model is based on a set of generic pAVM models (pAVM prototypes) and patient-specific pAVM models. The corresponding morphologic and mechanical properties are obtained from literature and MR-recordings of affected patients. Based on these vascular network models, the physics of blood flow is described with a lumped parameter model, while contrast agent (CA)-transport (substance transport) is modelled by solving the 1D advection-diffusion equation. With this, a hemodynamic characterization of different pAVM morphologies and their influence on CA-dynamics is obtained. The results are compared to diagnostic DSA recordings to identify diagnostic parameters, which allow determining the presence and specific type of pAVM.

Blood Flow Model

A lumped parameter model (LPM)¹¹ is used to study the global dynamics in a vascular network,⁹ where this network is divided into individual vessel compartments (lumped elements) considered as homogeneous units to compute spatially averaged blood pressures p and flow rates Q . This approach allows for fast computations also for patient-specific models involving complex pAVM networks.

A lumped T-network (Fig. 3a) is employed as a model for each vascular compartment,

$$\frac{\partial p_m}{\partial t} = \frac{1}{C}(Q_0 - Q_1) \quad (1)$$

$$\frac{\partial Q_0}{\partial t} = \frac{2}{L}(p_0 - p_m) - \frac{R}{L}Q_0 \quad (2)$$

$$\frac{\partial Q_1}{\partial t} = \frac{2}{L}(p_m - p_1) - \frac{R}{L}Q_1 \quad (3)$$

$$L = \frac{\rho l}{\pi r^2} \quad (5)$$

$$C = D\pi r^2 l \quad (6)$$

The parameters R , L , and C represent the local resistance to the flow due to fluid viscosity, the fluid inertia, and the vessel compliance, respectively; Q_0 , Q_1 , p_0 , and p_1 are the flow rates and pressures at the end-nodes; p_m represents the pressure at the intermediate point m of the T-network. For a parabolic velocity profile in compartments of constant circular cross-section, the values for R , L , and C are constant in time and depend only on vessel geometry (length l and radius r), fluid properties (kinematic viscosity ν and density ρ of blood) and vessel distensibility D .

$$R = \frac{8\rho\nu l}{\pi r^4} \quad (4)$$

The ordinary differential equations (Eqs. (1)–(3)) for each compartment are coupled to the neighboring compartments by enforcing conservation of mass and continuity of pressure,¹¹ which results in a large system of equations.

We use the Crank–Nicolson scheme⁷ for numerical integration in time to ensure numerical stability despite the wide range of parameter (R , L , and C) scales. Numerical accuracy has been ensured with a convergence study. The resulting linear system of equations is solved directly using LU-decomposition.¹⁷

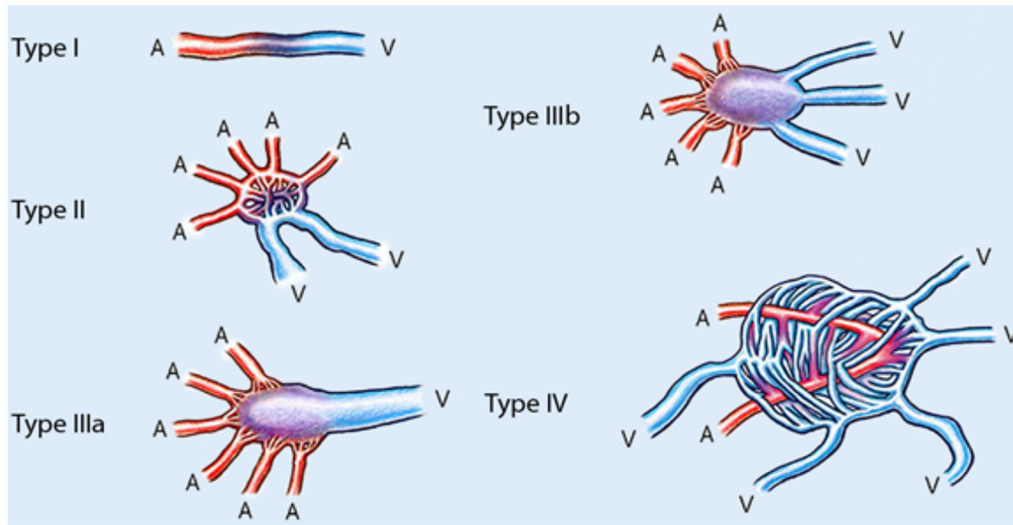


FIGURE 1. Yakes AVM classification system.³⁶

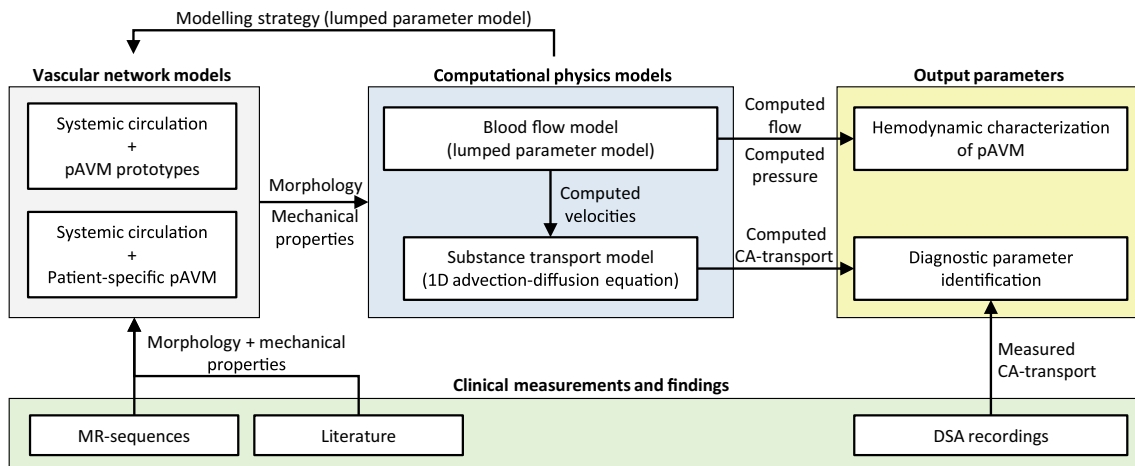


FIGURE 2. Modelling concept and workflow of the computational study.

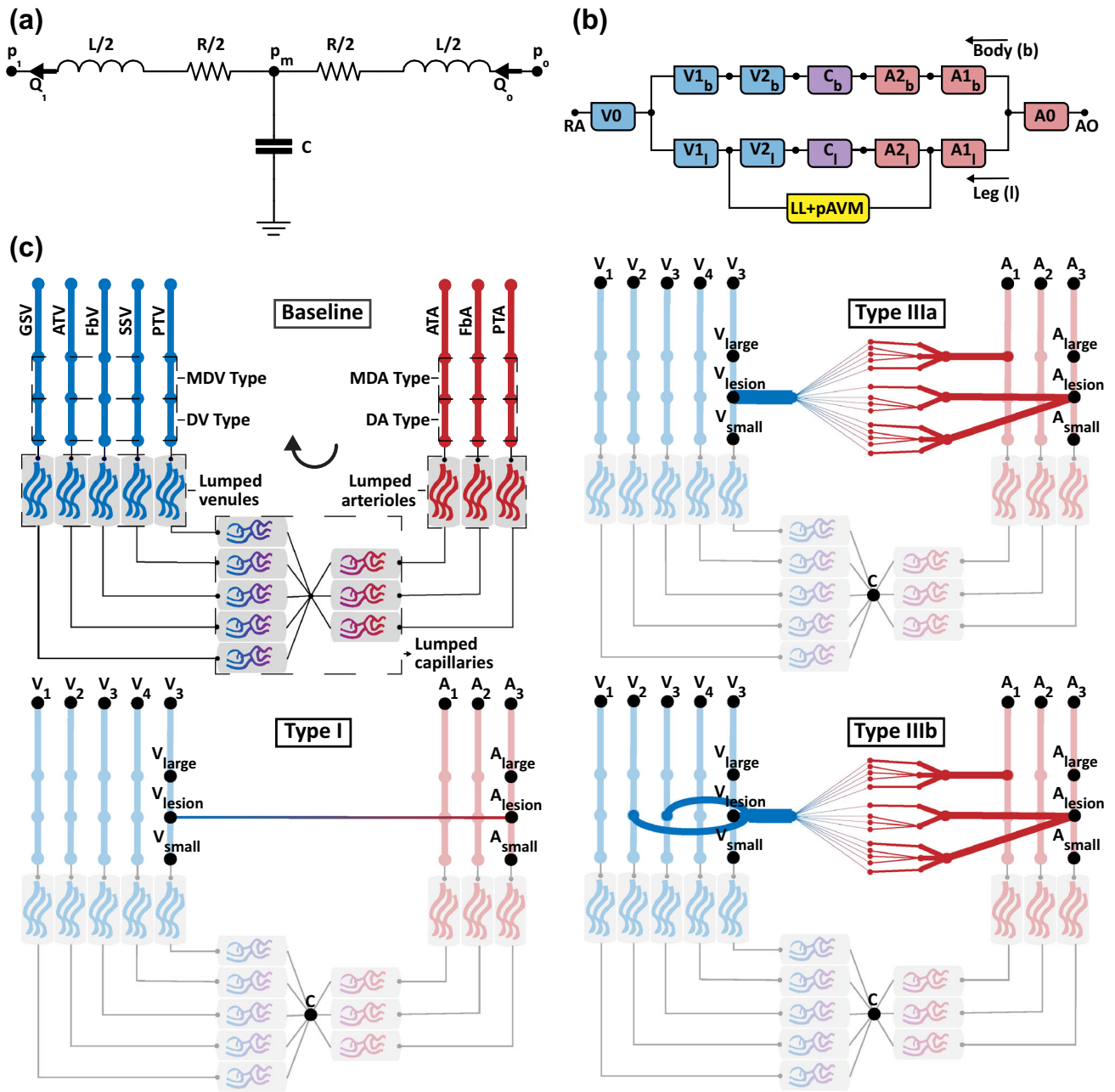


FIGURE 3. (a) Analogous electrical network representing one lumped element. R : resistance, L : inertiance, C : compliance.¹¹ (b) Adapted circulation model obtained from Ottesen *et al.*²⁷ (with elements A0–A2_{l/b}: large to small arteries, C_{l/b}: capillaries, V0–V2_{l/b}: large to small veins, LL: lower leg and foot vasculature). (c) LPM for the vasculature of the lower leg and foot (ATA/PTA and ATV/PTV: anterior/posterior tibial artery and vein, FbA/FbV: fibular artery/vein, MDA/MDV: medial and dorsal arteries/veins, DA/DV: digital arteries/veins and GSV/SSV: great/small saphenous vein) for baseline conditions and with pAVMs of types I, IIIa and IIIb. Black arrows indicate the principal direction of blood flow.

Prototype Vascular Network Models

A LPM for the vasculature of the lower leg and foot^{1,29} aims at representing realistic vascular components surrounding a lesion, including feeding arteries, draining veins, and a parallel microcirculation. The model comprises two types of lumped elements: (i) large and smaller pre-arteriolar and post-venular

arteries and veins and (ii) vessels pertaining to the microcirculation (Fig. 3c).

For the first type, values for R , L , and C are based on geometric and mechanical properties from literature.^{3,5,11,13,24,27,29,31,33} For the microcirculation, a full description of the microvascular network would lead to prohibitively high computational costs. A strongly simplified model is obtained by lumping bundles of

arterioles, capillaries, and venules into compartments. Values for R , L , and C were obtained from a lumped human circulation model²⁷ and scaled such that the resulting steady-state flow rate entering the lower leg corresponds to 25% of the flow entering the extremity,^{22,23} which comprises around 8% of the cardiac output (CO) in healthy subjects.⁸

At the level of the capillary bed, all open ends of arterioles and venules are connected *via* lumped elements with a central node (star network topology). The parameters $R_{c,j}$ and $C_{c,j}$ for each element j are obtained by evenly distributing the scaled capillary parameters from Ottesen *et al.*²⁷

$$R_{c,j} = R_c \zeta (1 - \zeta) N \quad (7)$$

$$C_{c,j} = \frac{C_c}{N} \quad (8)$$

where R_c/C_c is the total capillary resistance/compliance in the lower leg²⁷ and ζ is the proportion of arterial capillary elements with respect to the total number of capillary elements N .

Abnormal connections between arteries and veins in the foot are added corresponding to type I and type IIIa/b pAVMs (Figs. 1 and 3c).^{36,38} Dimensions and material properties of pAVM segments are chosen according to Yakes *et al.*,^{36,38} average values of the reported vessel types^{3,11,13} and measurements in diagnostic MR images.

In the following numerical experiments, the diameters of type I shunts and the aneurysmal vein of type IIIa/b pAVMs are varied within $d_{\text{shunt}} = 0.1\text{--}5$ mm and $d_{\text{aneurysm}} = 2\text{--}20$ mm. The distensibilities of the type I shunt D_{shunt} (Pa^{-1}) and of the aneurysmal vein of type IIIa/b pAVMs D_{aneurysm} (Pa^{-1}) are modified from typical arterial values¹³ to values beyond venous distensibilities.³

The presented LPM is embedded in a circulation model of the whole body²⁷ (Fig. 3b) by connecting nodes $A_1\text{--}A_3$ and $V_1\text{--}V_5$ in Fig. 3c to large arteries and veins of the circulation model. Our circulation model is partitioned into two parallel branches, representing the vessels in one leg (subscript l) and the rest of the circulation (subscript b).

A detailed list of employed dimensions and material properties can be found in the electronic supplementary material.

Aortic pressure waveforms are obtained from Goldberger *et al.*¹⁵ and Saeed *et al.*³² At the right atrium, a fixed pressure level of $p_{\text{RA}} = 5$ mmHg¹² is imposed.

Patient-Specific Vascular Network Model

Besides the networks shown in Fig. 3c, we also study an exemplary patient-specific pAVM model from an AVM registry (Division of Angiology, University Hospital Bern). The AVM registry is approved by the Ethics Committee of the Canton of Bern in Switzerland and patients signed a written informed consent. The spatial graph used to establish the LPM is obtained by semi-automatic segmentation and skeletonization (Amira 5.4.4., FEI Software, Hillsboro, Oregon, USA) of time-resolved subtraction gradient echo MR instances of the lesions. For simplicity, mechanical properties of these vessels are assumed to be constant with a distensibility of $D = 10^{-5} \text{ Pa}^{-1}$.¹³

Substance Transport Model

CA-transport is modelled by a one-dimensional advection–diffusion equation¹¹

$$\frac{\partial c}{\partial t} + u(x, t) \frac{\partial c}{\partial x} = D_{\text{Diff}} \frac{\partial^2 c}{\partial x^2} \quad (9)$$

with interpolated blood flow velocities $u(x, t)$ from the LPM network as advection velocities to compute the CA concentration $c(x, t)$. We use a constant diffusion coefficient $D_{\text{Diff,CA,Blood}} = 5 \times 10^{-9} \text{ m}^2/\text{s}$ for binary molecular diffusion of CA in blood.²¹

CA-transport through the microvasculature was not considered, since strong dispersion in the capillary bed arising from the wide variety of path lengths, results in effectively vanishing fluoroscopic venous CA-signals.

Nodes $A_1\text{--}A_3$ in Fig. 3c are chosen as CA injection sites, where a step function is applied as injection protocol. Venous outlet boundary nodes ($V_1\text{--}V_5$ in Fig. 3c) and arterial ends draining into the capillary bed are provided with convective outflow conditions.

Time integration of Eq. (9) is performed with a third-order, low-storage Runge–Kutta scheme.³⁵ The spatial derivative in the advection term is discretized with a first-order upwind finite difference scheme and the diffusion term with second-order central differences.⁶

Data Analysis and Diagnostic Parameters

For the hemodynamic analysis, volumetric flow rates and blood pressures are averaged over one cardiac cycle (Q_{mean} (ml/s) and P_{mean} (mmHg)). We define the pulsatility index P_{PI} (-) as the root-mean-square of the pressure fluctuations divided by the average pressure

$$P_{PI} = \frac{\sqrt{\frac{1}{N_t} \sum_{n=0}^{N_t} (p^{(n)} - P_{\text{mean}})^2}}{P_{\text{mean}}} \quad (10)$$

where N_t is the number of time steps in one cardiac cycle and $p^{(n)}$ the blood pressure at time $t^{(n)}$.

We characterize the CA-transport by determining the time of CA-arrival since injection start and the rate of increase (slope) of CA concentration upon arrival (cf. Figs. 5a and 5b) in our computational models and in diagnostic DSA recordings of exemplary pAVM cases.

The time of CA-arrival CA_{ToA} (s) is the elapsed time between injection start and the instant when 10% of the local peak concentration value CA_{max} (-) is reached. The slope CA_s (s^{-1}) is defined as the maximum time derivative of $c(x, t)$ (-) upon CA-arrival. To eliminate the effect of CA dilution at converging branching points, we also compute the “dilution-free” slope $CA_{s,\text{disp}} = CA_s / CA_{\text{max}}$ (s^{-1}). These values are determined at the nodes of computational models and on a pixel-by-pixel basis in DSA images.

RESULTS

Hemodynamic Characterization

Hemodynamic parameters of the baseline prototype without pAVM are shown in Fig. 4 for $d_{\text{shunt}} = 0$ mm. The baseline flow in a single artery below the knee (ATA, FbA, PTA) is 0.46 ml/s and baseline flow in a single large vein (ATV, PTV, GSV, SSV, FbV) of the lower leg is 0.27 ml/s. Arterial pressures are 70–80 mmHg, drop to 9–12 mmHg in the arterioles and the capillary bed and reach 7–8 mmHg in large veins in the lower leg. The baseline CO is 3.5 l/min with a systolic/diastolic pressure of 117/74 mmHg at the level of the ascending aorta. Total leg perfusion amounts to 0.27 l/min or 8% of CO.

Type I pAVM

Hemodynamic changes for a type I pAVM are depicted in the first column of Fig. 4 in function of d_{shunt} . A small shunt ($d_{\text{shunt}} = 0.1$ mm) has negligible effects on the surrounding vasculature. Increasing d_{shunt} results in increased arterial flow (up to seven-fold), an elevation of CO to 3.61 l/min and a reduced perfusion of distal vessels (arterial steal phenomenon). For $d_{\text{shunt}} \geq 5$ mm there remains nearly no arterial flow distal to the shunt.

Pressures in the arterial system are reduced with increasing d_{shunt} , while pressure in the venous system is increased.

Small veins returning from the microcirculation encounter elevated pressures resulting in impaired

draining of the capillary bed, which is manifested in reduced Q_{mean} at the location V_{small} (Fig. 4, top left). For larger shunts ($d_{\text{shunt}} \geq 2$ mm), P_{mean} in small veins surpasses the pressure in capillaries resulting in retrograde flow.

In general, the shunt reduces the pulsatility of the local arterial pressure. The greatest effect, however, is obtained on the venous side where pulsatility becomes significant for larger shunts ($d_{\text{shunt}} > 1$ mm).

Type III pAVM

Hemodynamic parameters for type IIIa pAVMs are shown in the second column of Fig. 4 in function of the aneurysm size d_{aneurysm} . The shunt causes increased arterial and venous flow rates in vessels proximal to the lesion and decreased flow rates in distal vessels. The increased demand for blood is distributed over two feeding arteries resulting in a four-fold increase in flow rate in each feeder for $d_{\text{aneurysm}} > 5$ mm, a ten-fold elevation of flow rates in the single draining vein and a concurrent CO increase to 3.6 l/min. Distal perfusion is halved and capillary drainage is impaired and disappears for $d_{\text{aneurysm}} > 2$ mm.

Arterial pressures drop by 5–9 mmHg and increase by 22–24 mmHg in the venous system for increasing d_{aneurysm} . Flow reversal in small veins and venules is a direct consequence of the elevation of venous pressure above capillary levels.

Interestingly, a significant dependence of Q_{mean} and P_{mean} on d_{aneurysm} is only observed for $d_{\text{aneurysm}} < 5$ mm. Increasing d_{aneurysm} beyond 5 mm leaves these quantities nearly unchanged.

P_{PI} is mostly affected in venous compartments, where it increases strongly for $d_{\text{aneurysm}} < 5$ mm. Further increase of d_{aneurysm} leads to a drop in P_{PI} nearly back to the baseline conditions.

Type IIIb pAVM

The behavior of the type IIIb pAVM (third column of Fig. 4) is similar to the type IIIa lesion. The main differences lie in the flow rates in the multiple draining veins: while we observe a ten-fold increase in Q_{mean} in the single draining vein for a type IIIa, this effect is less prominent for a type IIIb lesion, where only a five-fold increase is observed. In contrast to type IIIa, the pressure in small veins remains below capillary pressure levels for all d_{aneurysm} such that capillary drainage is preserved.

CA-Transport in pAVM Prototypes

Figures 5a and 5b illustrate the CA-transport for a type I pAVM with $d_{\text{shunt}} = 0.5$ mm and for a type IIIb pAVM with $d_{\text{aneurysm}} = 15$ mm. Values are sampled

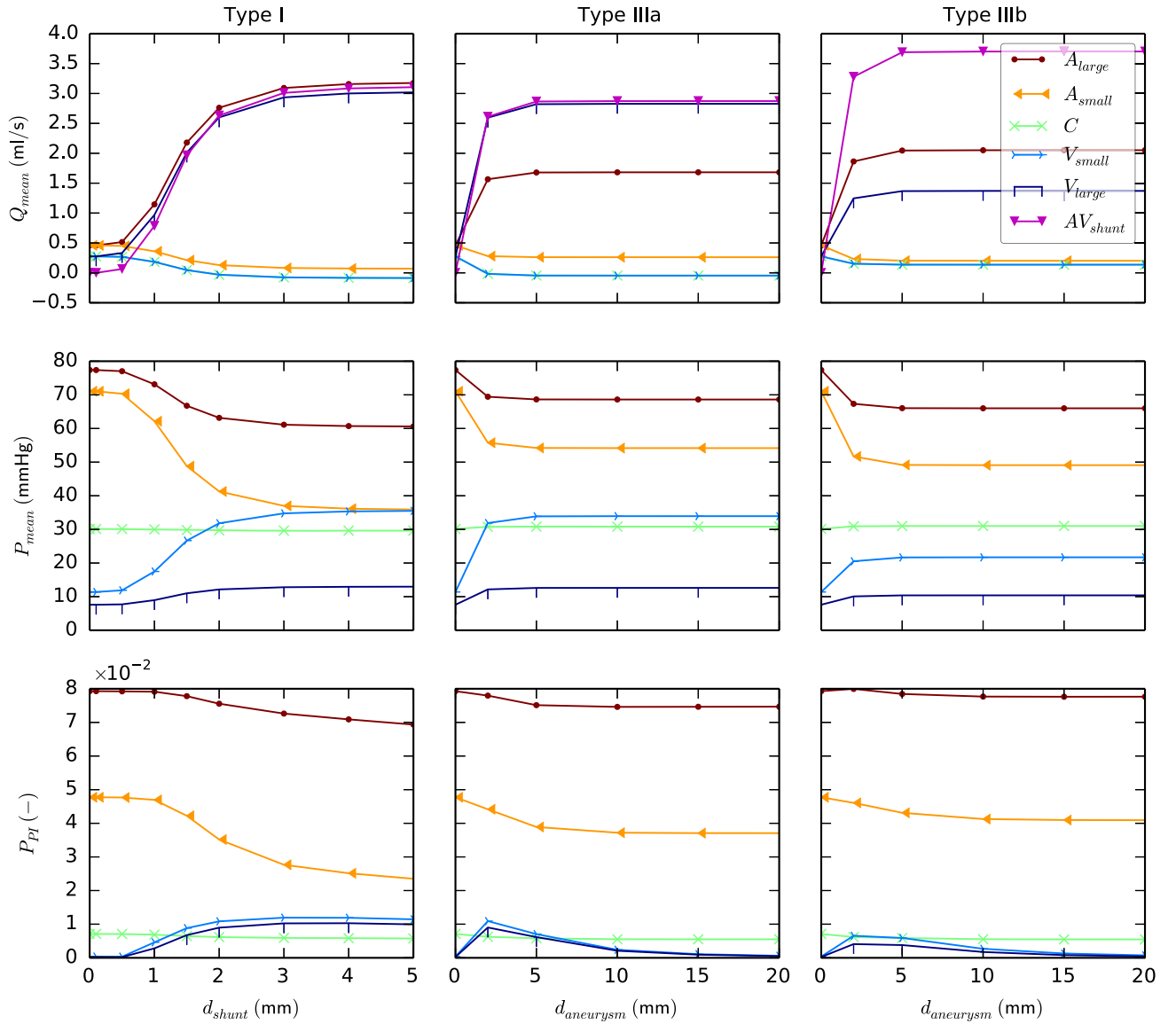


FIGURE 4. Q_{mean} (top row), P_{mean} (middle row) and P_{PI} (bottom row) in representative systemic vessels (points A_{large} , A_{small} , C , V_{small} , and V_{large} in Fig. 3c and AV_{shunt} representing the total shunt flow) for type I (first column), type IIIa (second column), and type IIIb (third column) prototype pAVMs for different d_{shunt} and d_{aneurysm} .

close to the injection site at A_{large} and at the arterial and venous ends of the lesion (A_{lesion} and V_{lesion}). Figure 5c summarizes the advective and the dispersive character of different pAVM configurations. To this end, the transit time $CA_{\text{transit}} = CA_{\text{ToA}}(V_{\text{lesion}}) - CA_{\text{ToA}}(A_{\text{lesion}})$, which is required for CA to pass through the lesions, is plotted against the relative change of $CA_{s,\text{disp}}$ across the lesion, computed as $CA_{s,\text{disp}}^{V/A} = CA_{s,\text{disp}}(V_{\text{lesion}})/CA_{s,\text{disp}}(A_{\text{lesion}})$.

Type I pAVMs exhibit significant CA concentration also on the venous side (which does not contain any CA in the non-pathological baseline model). CA-rich blood at the venous endpoint of the malformation is diluted with CA-free blood returning from the micro-

circulation, such that CA_{max} drops to 20% and CA_s is reduced by 85%. However, $CA_{s,\text{disp}}(V_{\text{lesion}})$ remains at a similar level as $CA_{s,\text{disp}}(A_{\text{lesion}})$. Figure 5c shows that type I exhibits a nearly size-independent, non-dispersive and fast shunting behavior for $0.5 < d_{\text{shunt}} < 4$ mm. For smaller diameters, CA_{transit} increases because of very low shunting flow rates. If d_{shunt} exceeds the diameter of adjacent systemic veins, a decrease of $CA_{s,\text{disp}}^{V/A}$ is observed.

Types IIIa/b (Fig. 5b) exhibit a completely different transport behavior in the venous compartments: $CA_{s,\text{disp}}(V_{\text{lesion}})$ is reduced by more than 80% compared to $CA_{s,\text{disp}}(A_{\text{lesion}})$. Direct comparison of type IIIa/b pAVMs with different d_{aneurysm} and D_{aneurysm}

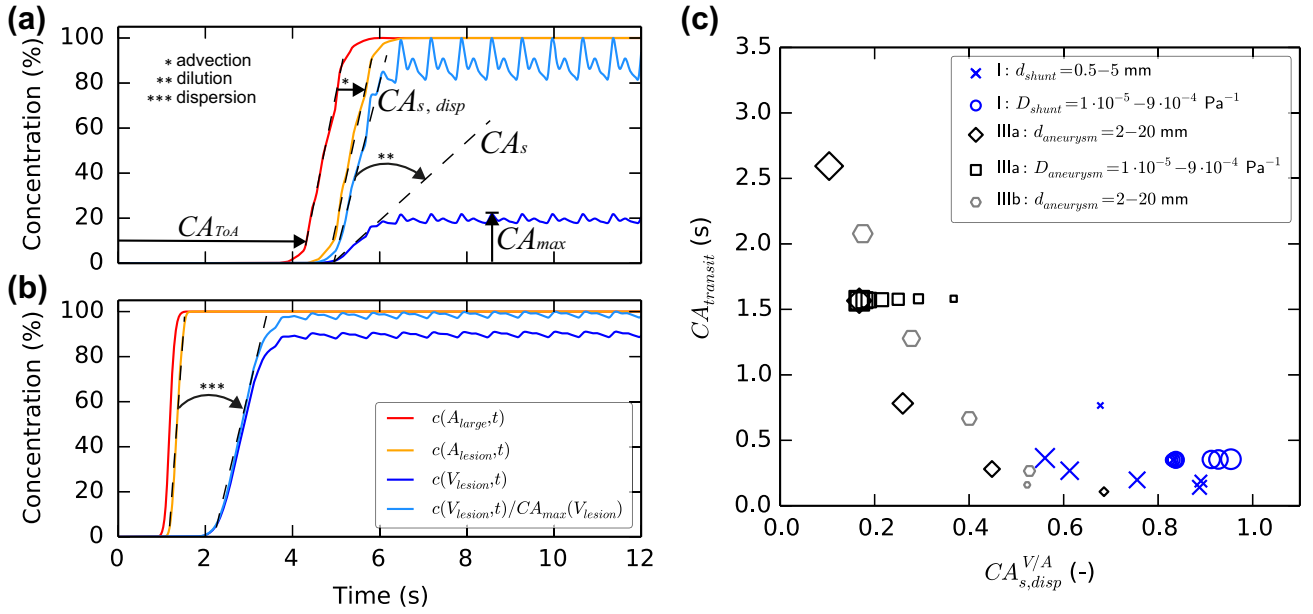


FIGURE 5. Temporal evolution of CA concentration at points A_{large} , A_{lesion} , and V_{lesion} for (a): Type I ($d_{shunt} = 0.5$ mm) and (b) Type IIIb ($d_{aneurysm} = 15$ mm) pAVMs. (c) Summary of CA-transport behavior over pAVM vessels for type I (blue), type IIIa (black), and type IIIb (grey) pAVM prototypes characterized by the relative change of slope $CA_{s, disp}^{V/A} = CA_{s, disp}(V_{lesion})/CA_{s, disp}(A_{lesion})$ and the transit time $CA_{transit} = CA_{ToA}(V_{lesion}) - CA_{ToA}(A_{lesion})$ for different characteristic shunt diameters d and distensibilities D (the marker size scales with the parameter ranges).

(Fig. 5c) shows that larger aneurysms result in a gradual reduction of $CA_{s, disp}^{V/A}$ and a concurrent increase in CA transit time.

For all pAVM types, varying the distensibility (while keeping the characteristic shunt diameter constant) does not affect $CA_{transit}$, but it results in minor alterations of $CA_{s, disp}^{V/A}$ (Fig. 5c).

In summary, our results show that $CA_{transit}$ tends to be larger and $CA_{s, disp}^{V/A}$ is smaller for types IIIa/b than for type I. Type IIIa and type IIIb prototypes do not exhibit major differences, except for a small shift in size-dependence.

CA-Transport in Patient-Specific Models and Diagnostic DSA

A similar analysis is performed for diagnostic DSA recordings. Normalized dispersive slopes, $CA_{s, disp}^{norm}$ (-), and normalized times of arrival, CA_{ToA}^{norm} (-), are shown for an exemplary type I (Fig. 6) and type IIIb (Fig. 7) case. At each pixel, $CA_{s, disp}$ is normalized with the maximum of $CA_{s, disp}$ over all frames. The values for CA_{ToA} are normalized with the total turnover time of CA in the considered sequence, defined as the time elapsed between injection start and the last 10%-CA-signal detection.

The results for type I show rapid CA-transport with nearly unchanged $CA_{s, disp}^{norm}$ (Fig. 6a). The correspond-

ing histogram (Fig. 6b) shows an accumulation of $CA_{s, disp}^{norm}$ towards large values close to $CA_{s, disp}^{norm}$ at the arterial injection site. The histogram for CA_{ToA}^{norm} (Fig. 6d) has a peak at small times of arrival. The corresponding image colored with CA_{ToA}^{norm} (Fig. 6c) shows that this peak represents the fast CA-transport within the artery and the nearly immediately following arrival of CA in the venous system.

Type IIIb (Fig. 7) shows an entirely different shunting behavior: the histogram of $CA_{s, disp}^{norm}$ (Fig. 7b) is broader and rather skewed to the right with a mean value far below the maximum arterial $CA_{s, disp}^{norm}$. The histogram for CA_{ToA}^{norm} (Fig. 7d) is characterized by: (i) an early sharp peak at $CA_{ToA}^{norm} \approx 0.1$ corresponding to fast CA-transport within the arterial system, (ii) the fast collection of CA within the aneurysmal vein resulting in the local minimum at $CA_{ToA}^{norm} \approx 0.2$, and (iii) a broader peak at $CA_{ToA}^{norm} \approx 0.6$ corresponding to a delayed distribution of CA into a large number of interconnected veins before being collected in large systemic veins (Fig. 7c).

Finally, we show our results for the patient-specific computational model (Fig. 8) corresponding to the type IIIb pAVM shown above. The diagnostic parameters are sampled at each node of the model. The resulting frequencies of the histogram bins are weighted with the sum of the axial cross-sectional areas of the associated blood vessel segments to obtain a spatial frequency measure proportional to the pixel-based

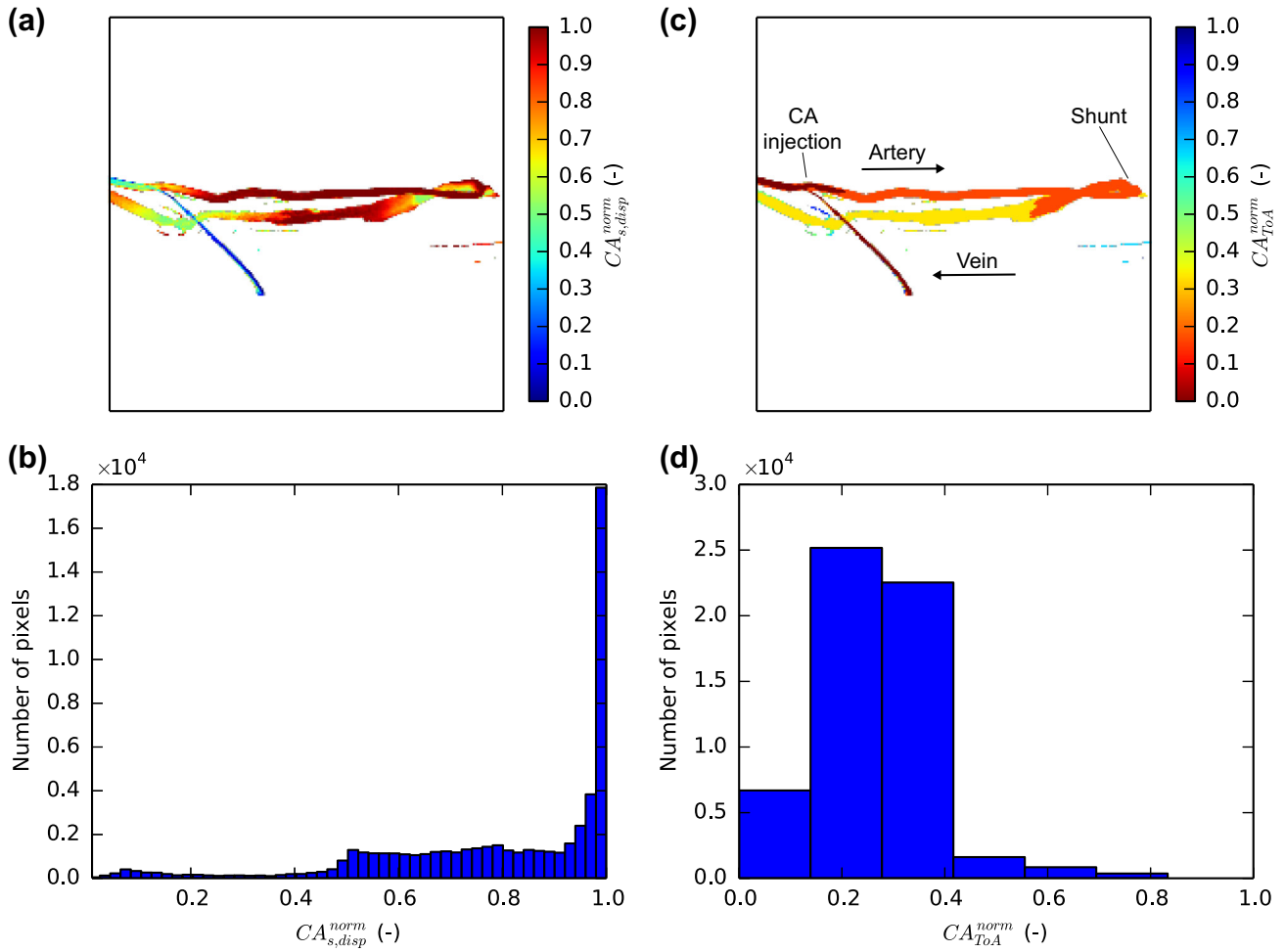


FIGURE 6. Spatial distribution of $CA_{s,disp}^{norm}$ (a) and CA_{ToA}^{norm} (c) and histogram representation of $CA_{s,disp}^{norm}$ (b) and CA_{ToA}^{norm} (d) for a type I lesion.

analysis of diagnostic DSA recordings. The weighted histograms for $CA_{s,disp}^{norm}$ (Fig. 8a) and CA_{ToA}^{norm} (Fig. 8b) show similar relative characteristics as the histograms in Figs. 7b and 7d, except for a more dispersive behavior evident in the lower $CA_{s,disp}^{norm}$ values and for a less prominent initial peak relative to the second maximum in CA_{ToA}^{norm} .

DISCUSSION

Hemodynamic Parameters in the Baseline Model

The baseline LPM with the circulation model was designed to represent a realistic vascular environment for pAVMs. Pressure levels in the arterial segments and in venules and small/large veins of the baseline LPM attain values conforming with average values reported in literature.²⁷ *In-vivo* flow rate values in the main vessels of the lower leg are only scarcely documented. According to Doppler ultrasound measure-

ments reported in Kalayci *et al.*,²⁴ flow rates in a tibial artery are in the range 0.3–0.4 ml/s and around 0.2 ml/s in the tibial veins, which is in good accordance with the flow rates of our baseline LPM (Fig. 4).

Hemodynamic Parameters in Type I pAVMs

The results show that type I pAVMs can have a significant impact on local vessel perfusion (Fig. 4). Ischemic tissue lesions are a clinical consequence of this pAVM type and are assumed to be caused by arterial steal.³⁰ Our model suggests that this effect is not only due to the preference of blood to follow the path of lowest resistance, but also due to the increase in venous pressure, which can ultimately suppress any kind of distal arterial forward flow. The biological response to the increase in venous pressure and the collateral increase in venous pulsatility can be an enlargement, thickening, and stiffening of veins, which is often observed in pAVM patients.¹⁸ Our model shows that the extent of this phenomenon strongly

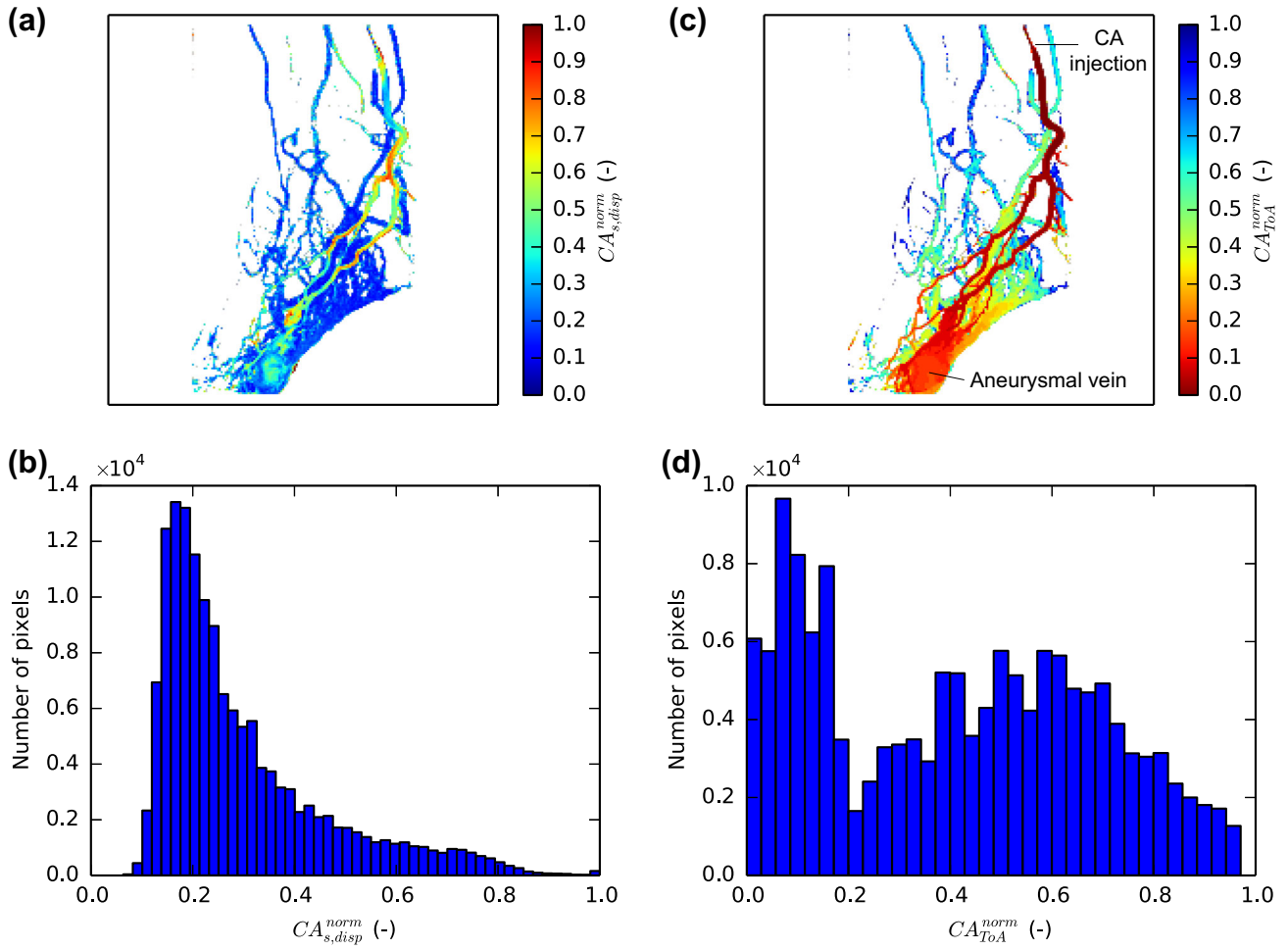


FIGURE 7. Spatial distribution of $CA_{s,disp}^{norm}$ (a) and CA_{ToA}^{norm} (c) and histogram representation of $CA_{s,disp}^{norm}$ (b) and CA_{ToA}^{norm} (d) for a type IIIb lesion.

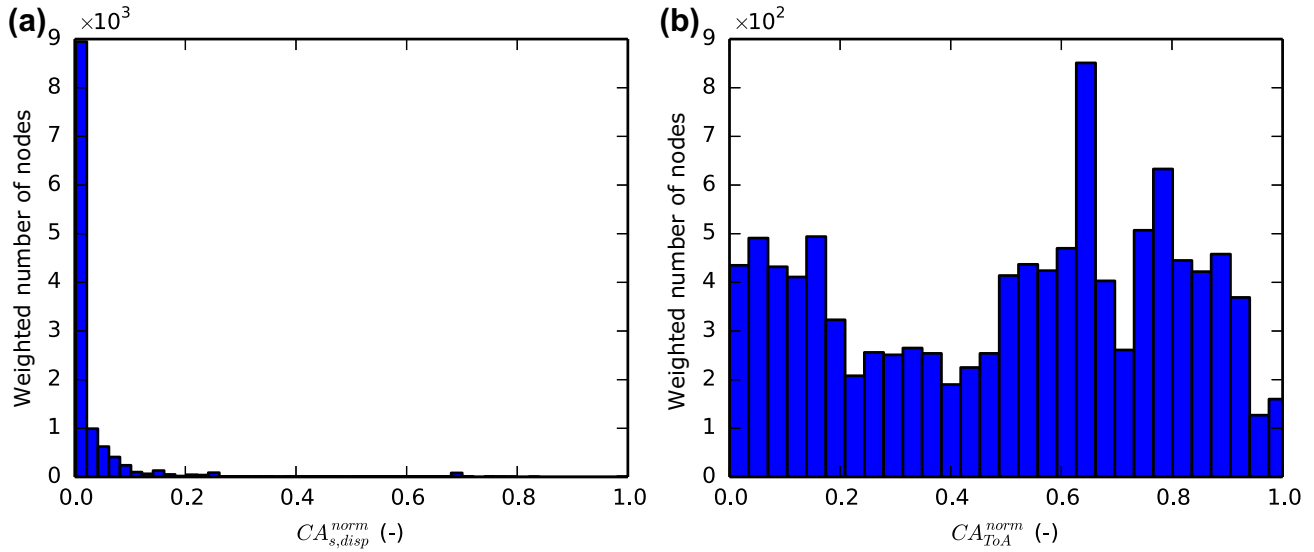


FIGURE 8. Weighted histograms for $CA_{s,disp}^{norm}$ (a) and CA_{ToA}^{norm} (b) for the patient-specific type IIIb model.

depends on the size (d_{shunt}) of the shunting vessel: the larger the shunt, the higher the reduction of distal perfusion. If d_{shunt} is comparable to the surrounding systemic arteries, distal perfusion cannot be maintained. For even larger shunt diameters, the altered hemodynamic environment can cause retrograde flow in distal veins.

Increased pulsatility in the venous system is a consequence of a lack of compliance capacity in the shunt. Interestingly, even increasing the distensibility of the shunting vessel far above physiological venous values is not sufficient to compensate for this lack of Windkessel-effect (cf. electronic supplementary material).

Hemodynamic Parameters in Type IIIa/b pAVMs

To analyze the impact of different manifestations of type IIIa pAVMs the aneurysm size, d_{aneurysm} , and distensibility, D_{aneurysm} , are varied, because the aneurysm in the type III pAVM may be prone to growth and structural weakness. Interestingly, the hemodynamic parameters depend on d_{aneurysm} only up to $d_{\text{aneurysm}} \approx 5$ mm. At this point, the connecting vein exceeds the typical diameter of systemic veins and no further aggravation of the hemodynamic consequences is observable. The origin of this limiting behavior is that a large aneurysm contributes only little to the overall flow resistance of the lesion (compared to small arteries and arterioles draining into the aneurysmal vein). Thus, further increase of d_{aneurysm} does not cause significant change in pressures or flow rates. Moreover, the relation between P_{PI} and d_{aneurysm} suggests that large aneurysmal veins ($d_{\text{aneurysm}} \geq 5$ mm) compensate for the lack of Windkessel-effect observed in type I lesions.

This suggests that an aneurysmatic enlargement of the draining vein could be driven by a vicious cycle of increasing flow and pressure levels and high pressure pulsatility. Once enlarged to a certain diameter, flow, and pressure stop increasing and pressure pulsatility decreases again such that the cycle is broken.

The similarity between the effects of type IIIa and IIIb pAVMs is expected, due to their resembling morphology. The observation that type IIIa pAVMs are more prone to exhibit lack of capillary drainage than type IIIb (cf. Fig. 4) is the only significant hemodynamic difference. Their separate classification is rather a consequence of technical and clinical aspects, such as the access for treatment, than due to their hemodynamic behavior.

CA-Transport

The influence of the shunt morphology on primary hemodynamic parameters (e.g. pressure and flow) is essential to characterize the lesions and identify opti-

mal treatment strategies (with respect to safety and efficacy). However, this influence is difficult to assess clinically. Therefore, this study focuses on parameters that can be obtained from diagnostic images, such as the rate of CA increase and the time of arrival of CA.

Results in Fig. 5 suggest that $CA_{\text{s,disp}}$ and CA_{ToA} show great potential in providing information to differentiate pAVM morphologies and sizes. Our type I prototype pAVM is characterized by a non-dispersive behavior, i.e., $CA_{\text{s,disp}}$ is only little affected by the malformation and remains at a similar level as CA passes from the arterial to the venous system. Type III malformations can be distinguished from type I lesions, due to their dispersivity. In both cases, the dispersive behavior is enhanced when the connecting vein is enlarged beyond systemic venous diameters. Since flow rates in type III malformations exhibit a limited dependence on the aneurysm size, large aneurysms can cause a drastic reduction in local flow velocity and a size-dependent increase in CA_{transit} . On the other hand, type I malformations exhibit relatively low CA_{transit} , independent of d_{shunt} .

Based on these observations, a similar separation of different pAVM types and sizes was targeted in diagnostic DSA recordings (Fig. 6 for type I and Fig. 7 for type IIIb).

Again, the distribution of $CA_{\text{s,disp}}^{\text{norm}}$ is a distinctive indicator for the dispersivity of the lesion. The accumulation of values towards large slopes and the left-skewed shape of the histogram of the type I malformation suggests that CA is shunted through one vessel. Malformations with a more dispersive behavior (type III), where CA is first distributed and then collected in smaller vessels before re-entering systemic veins, exhibit smaller global mean $CA_{\text{s,disp}}^{\text{norm}}$ values with a right-skewed distribution.

The distribution of $CA_{\text{ToA}}^{\text{norm}}$ provides further cues for the specific pAVM type. For direct shunts in large vessels (type I), $CA_{\text{ToA}}^{\text{norm}}$ values on the venous side are only slightly larger than arterial values, resulting in a single peak in the histogram at low values. For a type IIIb malformation, CA is first distributed in the arterial feeders (first, sharp peak), then collected in a single shunting aneurysm (local minimum) and distributed into a large number of draining veins (second peak). The large width of the second peak indicates a highly dispersive venous phase, characteristic for type IIIb morphologies, which contain multiple draining veins. Therefore, the number and the width of the peaks in $CA_{\text{ToA}}^{\text{norm}}$ histograms can serve as a further diagnostic marker of the pAVM type.

The consistency between *in vivo* observations and computational results introduces the possibility of employing morphological MR data to estimate CA-

transport and the corresponding parameters $CA_{s,disp}^{norm}$ and CA_{ToA}^{norm} computationally and without the need for minimally-invasive DSA sequences. Further research and validation steps are required to establish a patient-specific computational angiography tool that can replace the current fluoroscopic modality in the process of determining the presented diagnostic parameters. Alternatively, non-invasive and contrast-free angiography modalities (e.g. dynamic tagging MR-angiography¹⁰) may serve as a basis to determine diagnostic parameters, thereby minimizing the risks of the diagnostic intervention.

Summary

In summary, we have introduced a set of computational methods and prototype pAVM models that allow determining the hemodynamic consequences of different shunt morphologies on surrounding vascular components. A thorough characterization of type I and type IIIa/b lesions has been presented and brought into context with clinical observations. The analysis of CA-transport through different malformation types revealed a set of diagnostic parameters that show great potential in allowing an automated classification and characterization of pAVMs. To fully establish and confirm the potential of this novel diagnostic procedure, further research, validation and analysis of different manifestations of pAVMs has to be performed. In the future, the proposed methods can promote the development and refinement of diagnosis and treatment strategies, reduce complication rates and the number of misdiagnosed cases and may allow the identification of yet unknown malformation types.

ELECTRONIC SUPPLEMENTARY MATERIAL

The online version of this article (doi: [10.1007/s10439-017-1821-9](https://doi.org/10.1007/s10439-017-1821-9)) contains supplementary material, which is available to authorized users.

CONFLICT OF INTEREST

None.

REFERENCES

- ¹Agur, A. M. R., and A. F. Dalley. Grant's Atlas of Anatomy. Baltimore: Lippincott Williams & Wilkins, 2009, 884 pp.
- ²Al-Adnani, M., S. Williams, D. Rampling, M. Ashworth, M. Malone, and N. J. Sebire. Histopathological reporting of paediatric cutaneous vascular anomalies in relation to proposed multidisciplinary classification system. *J. Clin. Pathol.* 59:1278–1282, 2006.
- ³Bérczi, V., A. Á. Molnár, A. Apor, V. Kovács, C. Ruzics, C. Várallyay, K. Hüttl, E. Monos, and G. L. Nádasy. Non-invasive assessment of human large vein diameter, capacity, distensibility and ellipticity in situ: dependence on anatomical location, age, body position and pressure. *Eur. J. Appl. Physiol.* 95:283–289, 2005.
- ⁴Brouillard, P., and M. Vikkula. Vascular malformations: localized defects in vascular morphogenesis. *Clin. Genet.* 63:340–351, 2003.
- ⁵Chen, Y. G., P. A. Cook, M. A. McClinton, R. A. Espinosa, and E. F. Wilgis. Microarterial anatomy of the lesser toe proximal interphalangeal joints. *J. Hand Surg.* 23:256–260, 1998.
- ⁶Chung, T. J. Computational Fluid Dynamics. London: Cambridge University Press, 2014, 1058 pp.
- ⁷Crank, J., and P. Nicolson. A practical method for numerical evaluation of solutions of partial differential equations of the heat-conduction type. *Math. Proc. Camb. Philos. Soc.* 43:50–67, 1947.
- ⁸Dineno, F. A., P. P. Jones, D. R. Seals, and H. Tanaka. Limb blood flow and vascular conductance are reduced with age in healthy humans: relation to elevations in sympathetic nerve activity and declines in oxygen demand. *Circulation* 100:164–170, 1999.
- ⁹Erbertseder, K., J. Reichold, B. Flemisch, P. Jenny, and R. Helmig. A coupled discrete/continuum model for describing cancer-therapeutic transport in the lung. *PLoS ONE* 7:e31966, 2012.
- ¹⁰Essig, M., R. Engenhart, M. V. Knopp, M. Bock, J. Scharf, J. Debus, F. Wenz, H. Hawighorst, L. R. Schad, and G. van Kaick. Cerebral arteriovenous malformations: improved nidus demarcation by means of dynamic tagging MR-angiography. *Magn. Reson. Imaging* 14:227–233, 1996.
- ¹¹Formaggia, L., A. Quarteroni, and A. Veneziani. Cardiovascular Mathematics: Modeling and Simulation of the Circulatory System. Springer, Milan, 2010, 528 pp.
- ¹²Fuster, V., R. Walsh, and R. Harrington. Hurst's the Heart, 13th edn, Vol. 1. New York: McGraw-Hill Education/Medical, 2011, 2500 pp.
- ¹³Gamble, G., J. Zorn, G. Sanders, S. MacMahon, and N. Sharpe. Estimation of arterial stiffness, compliance, and distensibility from M-mode ultrasound measurements of the common carotid artery. *Stroke J. Cereb. Circ.* 25:11–16, 1994.
- ¹⁴Gao, E., W. L. Young, G. J. Hademenos, T. F. Massoud, R. R. Sciacca, Q. Ma, S. Joshi, H. Mast, J. P. Mohr, S. Vulliemoz, and J. Pile-Spellman. Theoretical modelling of arteriovenous malformation rupture risk: a feasibility and validation study. *Med. Eng. Phys.* 20:489–501, 1998.
- ¹⁵Goldberger, A. L., L. A. Amaral, L. Glass, J. M. Hausdorff, P. C. Ivanov, R. G. Mark, J. E. Mietus, G. B. Moody, C. K. Peng, and H. E. Stanley. PhysioBank, PhysioToolkit, and PhysioNet: components of a new research resource for complex physiologic signals. *Circulation* 101:E215–E220, 2000.
- ¹⁶Golovin, S. V., A. K. Khe, and K. A. Gadyshina. Hydraulic model of cerebral arteriovenous malformations. *J. Fluid Mech.* 797:110–129, 2016.
- ¹⁷Golub, G. H. Matrix Computations. Baltimore: Johns Hopkins University Press, 2013, 756 pp.
- ¹⁸Griessenauer, C. J., P. Dolati, A. Thomas, and C. S. Ogilvy. Arteriovenous malformations: how we changed our

- practice. In: *Controversies in Vascular Neurosurgery*, edited by E. Veznedaroglu. Cham: Springer, 2016, pp. 157–164. doi:[10.1007/978-3-319-27315-0_14](https://doi.org/10.1007/978-3-319-27315-0_14).
- ¹⁹Hademenos, G. J., and T. F. Massoud. Risk of intracranial arteriovenous malformation rupture due to venous drainage impairment. A theoretical analysis. *Stroke J. Cereb. Circ.* 27:1072–1083, 1996.
 - ²⁰Hademenos, G. J., T. F. Massoud, and F. Viñuela. A biomathematical model of intracranial arteriovenous malformations based on electrical network analysis: theory and hemodynamics. *Neurosurgery* 38:1005–1014, 1996; (discussion 1014–1015).
 - ²¹Hao, Q., and B. B. Lieber. Dispersive transport of angiographic contrast during antegrade arterial injection. *Cardiovasc. Eng. Technol.* 3:171–178, 2012.
 - ²²Holland, C. K., J. M. Brown, L. M. Scoutt, and K. J. Taylor. Lower extremity volumetric arterial blood flow in normal subjects. *Ultrasound Med. Biol.* 24:1079–1086, 1998.
 - ²³Hussain, S. T., R. E. Smith, R. F. Wood, and M. Bland. Observer variability in volumetric blood flow measurements in leg arteries using duplex ultrasound. *Ultrasound Med. Biol.* 22:287–291, 1996.
 - ²⁴Kalayci, T. O., F. Sonmezgoz, M. Apaydin, M. F. Inci, A. F. Sarp, B. Birlik, M. E. Uluç, O. Oyar, and M. Kestelli. Venous flow volume measured by duplex ultrasound can be used as an indicator of impaired tissue perfusion in patients with peripheral arterial disease. *Med. Ultrason.* 17:482–486, 2015.
 - ²⁵Madani, H., J. Farrant, N. Chhaya, I. Anwar, H. Marmery, A. Platts, and B. Holloway. Peripheral limb vascular malformations: an update of appropriate imaging and treatment options of a challenging condition. *Br. J. Radiol.* 88:20140406, 2015.
 - ²⁶Orlowski, P., P. Summers, J. A. Noble, J. Byrne, and Y. Ventikos. Computational modelling for the embolization of brain arteriovenous malformations. *Med. Eng. Phys.* 34:873–881, 2012.
 - ²⁷Ottesen, J. T., M. S. Olufsen, and J. K. Larsen. *Applied Mathematical Models in Human Physiology*. Philadelphia: Society for Industrial and Applied Mathematics, 2004, 184 pp.
 - ²⁸Pollak, Y., B. T. Katzen, and W. Pollak. High-output congestive failure in a patient with pulmonary arteriovenous malformations. *Cardiol. Rev.* 10:188–192, 2002.
 - ²⁹Ricci, S., L. Moro, and R. Antonelli Incalzi. The foot venous system: anatomy, physiology and relevance to clinical practice. *Dermatol. Surg.* 40:225–233, 2014.
 - ³⁰Richter, G. T., and A. B. Friedman. Hemangiomas and vascular malformations: current theory and management. *Int. J. Pediatr.* 2012:e645678, 2012.
 - ³¹Sabatier, M. J., L. Stoner, M. Reifemberger, and K. McCully. Doppler ultrasound assessment of posterior tibial artery size in humans. *J. Clin. Ultrasound (JCU)* 34:223–230, 2006.
 - ³²Saeed, M., M. Villarroel, A. T. Reisner, G. Clifford, L.-W. Lehman, G. Moody, T. Heldt, T. H. Kyaw, B. Moody, and R. G. Mark. Multiparameter intelligent monitoring in intensive care II (MIMIC-II): a public-access intensive care unit database. *Crit. Care Med.* 39:952–960, 2011.
 - ³³Szpinda, M. An angiographic study of the anterior tibial artery in patients with aortoiliac occlusive disease. *Folia Morphol.* 65:126–131, 2006.
 - ³⁴Tasnádi, G. Epidemiology and etiology of congenital vascular malformations. *Semin. Vasc. Surg.* 6:200–203, 1993.
 - ³⁵Williamson, J. H. Low-storage Runge–Kutta schemes. *J. Comput. Phys.* 35:48–56, 1980.
 - ³⁶Yakes, W., and I. Baumgartner. Interventional treatment of arterio-venous malformations. *Gefässchirurgie* 19:325–330, 2014.
 - ³⁷Yakes, W. F. Endovascular management of high-flow arteriovenous malformations. *Semin. Interv. Radiol.* 21:49–58, 2004.
 - ³⁸Yakes, W. F., and A. M. Yakes. Classification of arteriovenous malformation and therapeutic implication. In: *Hemangiomas and Vascular Malformations*, edited by R. Mattassi, D. A. Loose, and M. Vaghi. Milan: Springer, 2015, pp. 263–276. doi:[10.1007/978-88-470-5673-2_33](https://doi.org/10.1007/978-88-470-5673-2_33).